Journal of Materials Chemistry A

ROYAL SOCIETY OF CHEMISTRY

PAPER

View Article Online
View Journal | View Issue

Cite this: J. Mater. Chem. A, 2024, 12, 26902

Mass transport control over a conductive MOF 3D thin film to improve gas sensing†

Yu Pan,‡[ac] Wei Sun,‡[a] Junxiang Chen,[a] Yuan Lin,[a] Yong-Jun Chen,*[ab] Zhenhai Wen *[a] and Gang Xu *[abc]

Received 13th July 2024
Accepted 5th September 2024

DOI: 10.1039/d4ta04855e

rsc.li/materials-a

Mass transport in a c-MOF thin film has a significant impact on various chemical applications. However, a systematic study of the influence of the microstructure of c-MOF thin films on mass transport has not yet been conducted. In this work, a finite element method simulation model was used to explore the influence of the microstructure of a MOF 3D thin film on mass transport, with the aim of improving the performance of MOF thin films applied in heterogeneous reactions. The model reveals the relationship between the morphology-induced effective diffusion area and mass transfer efficiency in the film. As a proof of concept for the simulation model, Cu-HHTP was coated on ZnO-NWAs to form 3D thin films with different microstructures and their NH_3 sensing performance was evaluated. The results show that the Cu-HHTP 3D thin film with a thickness of ~20 nm, a height of ~3 μm and a density of 85% exhibits the highest response. This is attributed to the optimal effective diffusion area provided by this microstructure to improve the mass transfer efficiency in the 3D thin film, which aligns well with the theoretical model. This work opens an avenue for designing high-performance MOF 3D thin films for heterogeneous reactions.

Introduction

Conductive metal–organic framework (c-MOF) materials have gained significant attention recently due to their unique combination of porosity and conduction.[1–9] These properties make c-MOFs applicable to electronics,[10] energy storage,[11] catalysis[12] and chemical sensing,[13,14] where efficient charge and mass transport are critical. There have been efforts to improve the charge transport properties of c-MOFs through various methods, such as doping with guest molecules,[15] tuning the intralayer π-extended conjugation of c-MOFs[16,17] and preparing high-quality thin films.[18–21] Research on improving the mass transport of c-MOFs is significant for heterogeneous reactions, but is relatively less reported. Preparing c-MOFs into thin films by layer-by-layer (LBL) or other methods on a flat substrate has been identified as an effective solution to shorten the pathway for mass transport to improve the efficiency of heterogeneous reactions.[22–25] However, the number of active sites and the efficiency of mass transport remain limited by the restricted surface area of c-MOF 2D thin films.[26–32] To overcome these issues, a microstructure modulation strategy for the thin film was proposed in our previous work,[33,34] where a Cu-HHTP (Cu-2,3,6,7,10,11-hexahydrotriphenylene) thin film was grown using LBL on a nanowire-structured substrate to form a 3D thin film.[33,34] Compared to a Cu-HHTP 2D thin film, a 3D thin film was hypothesized to have a higher surface area, more active sites, and faster mass transport, leading to a 1000 times optimized limit of detection, 250% enhanced response, and a 130% improved response speed in NH_3 detection. However, the mechanism by which the microstructure of c-MOF thin films influences mass transport has not been explored. The density, height, and thickness of the 3D thin film can have a significant impact on mass transport and diffusion flux, which in turn affect various heterogeneous reactions (Scheme 1a). Understanding the influence of these factors on properties is crucial for designing and synthesizing high-performance c-MOF materials for heterogeneous reactions. To the best of our knowledge, this aspect has not been studied yet.

Herein, in order to investigate the influence of the microstructure of a c-MOF 3D thin film on mass transport in heterogeneous reactions, a combination of theoretical simulation and experimental testing was employed. Firstly, a simulation model based on Fick's law using the finite element method was built (Scheme 1b) to simulate the mass transport process and explore the relationship between the microstructure of the 3D thin film (including density, height and thickness) and gas

[a]State Key Laboratory of Structural Chemistry, Fujian Institute of Research on the Structure of Matter, Chinese Academy of Sciences, Fuzhou, Fujian 350002, P. R. China. E-mail: chenyongjun@fjirsm.ac.cn; Wen@fjirsm.ac.cn; gxu@fjirsm.ac.cn

[b]Fujian Science & Technology Innovation Laboratory for Optoelectronic Information of China, Fuzhou, Fujian 350108, P. R. China

[c]University of Chinese Academy of Sciences (UCAS), Beijing 100049, P. R. China

† Electronic supplementary information (ESI) available: The finite element method simulation, synthesis, IR, SEM, *I–V*, and sensing property tests. See DOI: https://doi.org/10.1039/d4ta04855e

‡ These authors contributed equally to this paper.

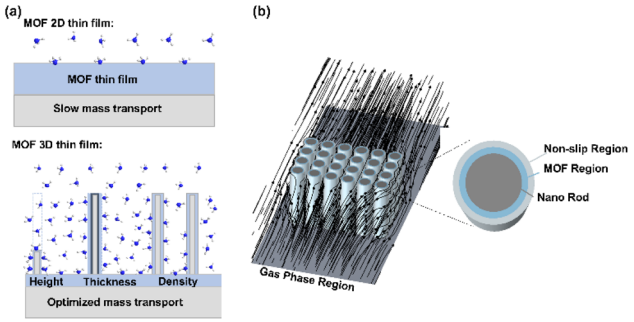

Scheme 1 (a) Differences in mass transfer between the MOF 2D thin film and MOF 3D thin film. (b) Schematic of the model used in finite element method simulation. The model is divided into four regions: the nanorod, the MOF region, the non-slip region, and the gas phase region. Different diffusion coefficients are used to represent each region (for details see the ESI†). The black color indicates the direction of streamline flow.

adsorption efficiency. The results of this simulation provided valuable insights for designing a microstructure with high mass transport efficiency in c-MOF 3D thin films used in heterogeneous reactions. According to the theoretical model, Cu-HHTP was grown on a ZnO nanowire array using an LBL method to form 3D thin films (denoted as a Cu-HHTP 3D thin film) with different thicknesses (0, ~5, ~20 and ~35 nm), heights (0.05, ~1, ~2 and ~3 μm) and densities (70%, 85%, 90% and 95%). The NH_3 sensing performances of these Cu-HHTP 3D thin films showed that the Cu-HHTP thin film with a thickness of ~20 nm, a height of ~3 μm and a density of 85% exhibits the highest response. This result was in good agreement with the theoretical model, confirming its validity and demonstrating the viability of the approach.

Finite element method simulation results

We employ Fick's laws of diffusion to describe the gas adsorption process, which is closely related to mass transport. The model takes into account three distinct phases: the gaseous phase, the c-MOF phase, and the non-slip zone at the interface between gas and c-MOF (as depicted in Scheme 1b). Each phase corresponds to a unique diffusion coefficient. Among them, the diffusion coefficient is the highest in the gaseous phase and the lowest in the c-MOF phase. The diffusion coefficient of the non-slip zone lies in between these two values, as it possesses certain characteristics of the gaseous phase while also being influenced by the frictional forces of the c-MOF phase. Therefore, gas diffusion in the non-slip zone may be constrained by various factors, such as morphology, adsorption site, *etc.*

To better understand gas diffusion in the non-slip zone, we conducted a qualitative analysis based on this model. Since gas diffusion is facile in the gaseous phase but becomes challenging near non-slip surfaces, the diffusion layer can easily advance but stagnate at the surface of the non-slip surface. According to the definition of the diffusion layer, the gas concentration within this layer is consistent across different microstructures. The kinetics of gas passing through the non-slip region and entering the interior of c-MOF are similar, which is attributed to the fact that the thickness of the slip plane, the diffusion coefficients of the slip plane, and c-MOF do not vary with changes in the microstructure. Therefore, the adsorption capacity of c-MOF per unit of time is controlled by the surface area composed of the diffusion layer. A larger area means more pathways for gas diffusion, resulting in a faster reaction process. We refer to this surface as the "effective diffusion surface" for qualitative analysis of this model. Since the diffusion layer stagnates at the surface of the non-slip area, we can merge the surfaces of non-slip areas with different microstructures to form an "effective diffusion surface". To illustrate this, we take a c-MOF 3D thin film with different thicknesses as an example. As shown in Scheme 2, the impact of the microstructure on the effective diffusion surface is revealed. For short periods of gas adsorption, increasing the thicknesses of the c-MOF layer enlarges the surface area of the nanorod, initially increasing the effective diffusion area. When the c-MOF layer thickness continues to increase, the effective diffusion area decreases to reduce the NAC. However, with the increase of adsorption time to more than 6 min, some gases can diffuse into occluded areas of space, such as the central area of four nanowires (Scheme 2, right), increasing the effective diffusion area to induce a higher NAC. Therefore, theoretical calculation shows that the gas adsorption quantity of the c-MOF 3D thin film first increases and then decreases before 6 min (Fig. 1). These discussions suggest that the surface area of the effective diffusion surface can serve as a descriptor for the gas adsorption quantity. It provides a qualitative analysis of the model and helps us understand the impact of the microstructure on mass transport in c-MOF thin films.

We altered the height, density and thickness of c-MOF 3D thin films in the model to simulate the influence of the microstructure of c-MOF 3D thin films on mass transport from the gaseous phase to the surface and gas adsorption. Fig. 1 presents the time-dependent concentration profiles in the gas phase and c-MOF region, along with the curves of time-dependent molecular capture quantities derived through integration over the c-MOF region. The adsorption quantity is

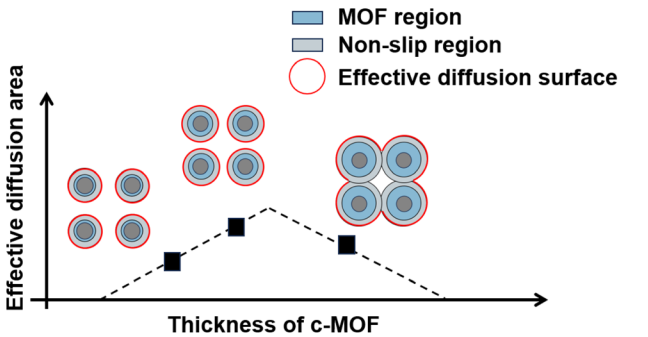

Scheme 2 The relationship between the thickness of the c-MOF and the area of the effective diffusion surface. The effective diffusion surface is marked with a red line. The colours of the other parts are consistent with those shown in Scheme 1.

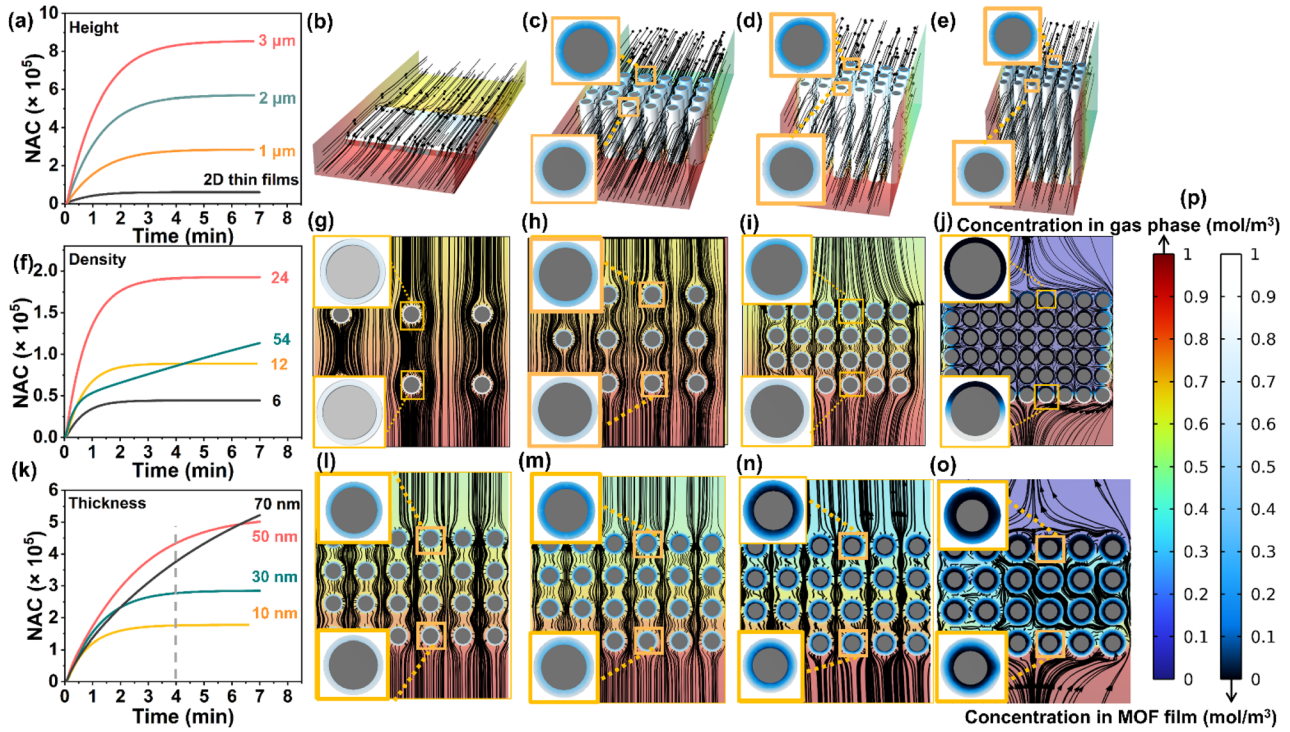

Fig. 1 The relationships between the height (a–e), density (f–j), and thickness (c–o) of 3D MOF thin films, and the time-varying molecular adsorption quantities, respectively. (a, f and k) The time-dependent molecular capture quantities in the system, with NAC represented for the number of atoms captured. The color maps provided indicate the situation at 0.7 minutes. For the complete data, please refer to Audio Videos Interactive S1–S3.† (p) Reference of color maps. In these color maps, the Jet Color Scheme (left color bar) represents the concentration in the gas phase region (unit: mol m^{-3}), and the Aurora Borealis Color Scheme represents the adsorption concentration within the MOF. The diffusion trajectories of the gas are represented by the black streamlines; the denser these lines are, the greater the gradient and the faster the diffusion speed. Except for (b), for each concentration distribution, an enlarged view is provided to distinctly display the concentration distribution within the MOF region facing towards and away from the airflow direction.

positively correlated with the height of the c-MOF 3D thin film (Fig. 1a–e and Audio Video Interactive S1†). However, when it comes to density and thickness, the adsorption quantity of the c-MOF 3D thin film increased firstly, reaching a maximum, and then decreased, indicating an optimal density or thickness for gas adsorption (Fig. 1f–o, Audio Video Interactive S2 and S3†). These results of the theoretical calculation could be explained by the concept of the effective diffusion surface. Different microstructures of c-MOF 3D thin films result in different effective diffusion surfaces, which in turn affect the mass transport. This optimization of gas adsorption in c-MOF 3D thin films with varying heights, densities, and thicknesses is illustrated in Fig. 1.

It is worth noting that our descriptor here specifically refers to the surface area, not the commonly referenced surface-to-volume ratio. A simple counterexample is the case of a single nanorod: as the nanorod thickens, the surface-to-volume ratio decreases, but the signal increases. Meanwhile, the area of the effective diffusion surface increases (Fig. S1†). Additionally, we discussed the off-axis flow and found its impact to be relatively minor (Fig. S2, for details see the ESI†). To correspond with the experiments, we also conducted tests on the distortion of the tilted model and found that it had minimal impact, with almost no noticeable changes (Fig. S3†).

Experimental results and discussion

As a proof of concept, Cu-HHTP 3D thin films with different thicknesses, heights, and densities were prepared by LBL coating a Cu-HHTP thin film on a ZnO nanowire array (ZnO-NWA) template.[33] The scanning electron microscopy (SEM) images of ZnO-NWA and Cu-HHTP 3D thin films on a sapphire substrate are shown in Fig. 2a. The morphologies of the Cu-HHTP 3D thin film exhibit are similar to those of the ZnO-NWs (Fig. 2a). However, the transmission electron microscopy (TEM) images of Cu-HHTP 3D thin films showed a core–sheath microstructure in Fig. 2b. By controlling the number of dipping cycles, uniform, continuous and crystalline Cu-HHTP thin films with different thicknesses (0, ~5, ~20 and ~35 nm) were obtained (Fig. 2a and b). The synthesis of ZnO-NWAs allowed us to design templates with different heights and densities (Fig. S4†).[35] By adjusting the height and density of the ZnO-NWA templates, the height and density of Cu-HHTP 3D thin films could be controlled respectively (Fig. 2c, d and S5 and S6†). As shown in Fig. 2c, the different heights of the Cu-HHTP 3D thin film, ranging from 0 to ~3 μm, were obtained. The densities were also gradually regulated from sparse (70%) to dense (95%), as confirmed by SEM images (Fig. 2d and S5†). Using ImageJ software, the space ratio of the nanowires was roughly

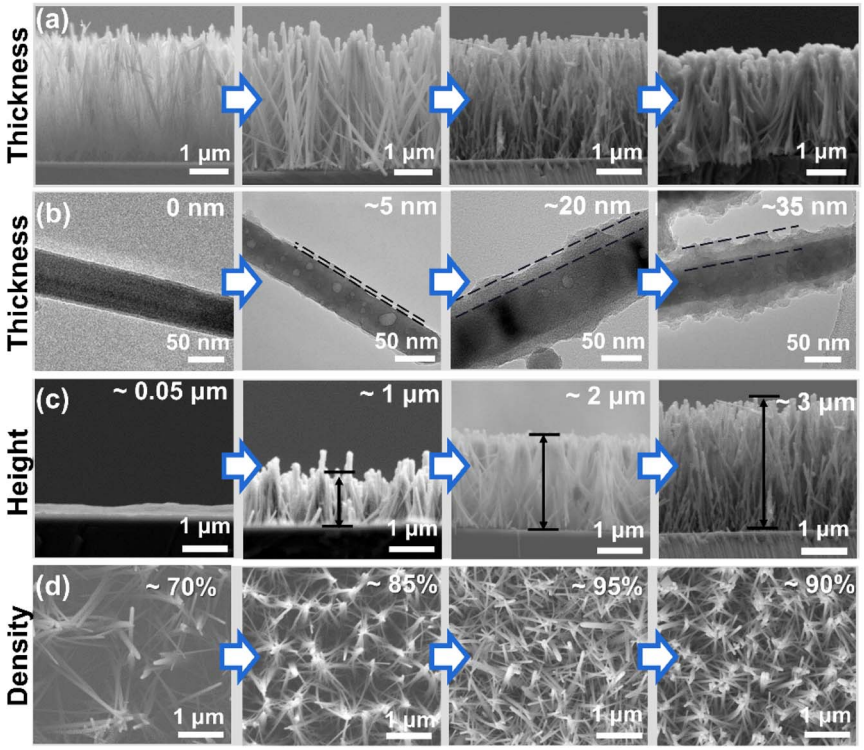

Fig. 2 SEM (a) and TEM (b) of 3D Cu-HHTP grown on a ZnO-NWA substrate with different thicknesses; SEM of 3D Cu-HHTP grown on a ZnO-NWA substrate with different heights (c) and densities (d).

measured, and the density can be roughly quantified to be 70–95% (Fig. S7, for details see the ESI†).

To prove the presence of the Cu-HHTP 3D thin film layer on the ZnO-NWA template, PXRD, Fourier-transform infrared (FT-IR) and Raman spectroscopy have been conducted. With the increase of film thickness, PXRD demonstrated that Cu-HHTP grew on the ZnO template with obvious crystallization (Fig. 3a). The FT-IR spectrum shows the peaks of the Cu-HHTP 3D thin film are similar to those of the as-prepared Cu-HHTP powder (Fig. S8†). Compared with HHTP, the C=C stretching vibration peak of Cu-HHTP powder disappeared at 1539 cm^{-1} and strengthened at 1445 cm^{-1}, indicating the successful coordination of Cu^{2+} and HHTP in Cu-HHTP powder. In the Raman spectrum, the main peaks at 1366, 1466, and 1545 cm^{-1} were attributed to the Cu-HHTP 3D thin film, along with other weak peaks attributed to ZnO (Fig. 3b). This evidence illustrated that the Cu-HHTP thin film was successfully formed on the ZnO-NWA template.

To confirm the continuity of the Cu-HHTP thin film on ZnO NWAs, we explored the electrical properties of the Cu-HHTP 3D thin film. Conductive devices were fabricated by connecting a pair of parallel electrodes attached to both edges of the Cu-HHTP thin film, where there were no ZnO-NWAs, ensuring that only the Cu-HHTP thin film was used as the conductive layer (Fig. S9†). As shown in Fig. 3c, the current–voltage (*I–V*) curve of the Cu-HHTP 3D thin film was linear and passed through the origin. At 5 V, the current was measured to be 10^{-9} A for the Cu-HHTP 3D thin film device. In contrast, the pristine device, where the electrodes were not in contact with the ZnO-NWA template, remained in a non-conducting state (Fig. 3c). In addition, the current of pure ZnO-NWAs was 10^{-6} A at 5 V (Fig. S10†), which was significantly different from that of the Cu-HHTP 3D thin film device. These results indicated that the Cu-HHTP thin film grew continuously on ZnO-NWAs, dominating the carrier transport of the device.

By optimizing the thicknesses, heights and densities of the Cu-HHTP 3D thin film, we aimed to improve the mass transport efficiency, which would enhance the performance of the film in various chemical applications, such as gas sensing (Fig. 1). To investigate the influence of the Cu-HHTP 3D thin film microstructure on mass transport efficiency, we conducted chemiresistive gas sensing experiments using a home-made system.[36] The devices made from the obtained Cu-HHTP 3D thin films exhibited a significant decrease in current and concentration-dependent responses to NH_3 (Fig. S11–S13†). The response behavior observed in this work is consistent with previously reported Cu-HHTP powder/films.[33,34] Firstly, Cu-HHTP 3D thin films with thicknesses of 0, ~5, ~20 and ~35 nm were studied for their response to NH_3 (Fig. 3d and S11†). When increasing the Cu-HHTP thin film thickness, the response values of the Cu-HHTP 3D thin film initially to 100 ppm NH_3 increased first and then decreased (Fig. 3d). The response value reaches a maximum at a Cu-HHTP thickness of ~20 nm. This trend can be explained by the fact that a thicker Cu-HHTP thin film provided more gas adsorption sites, leading to enhanced sensitivity. However, the increased thickness also results in

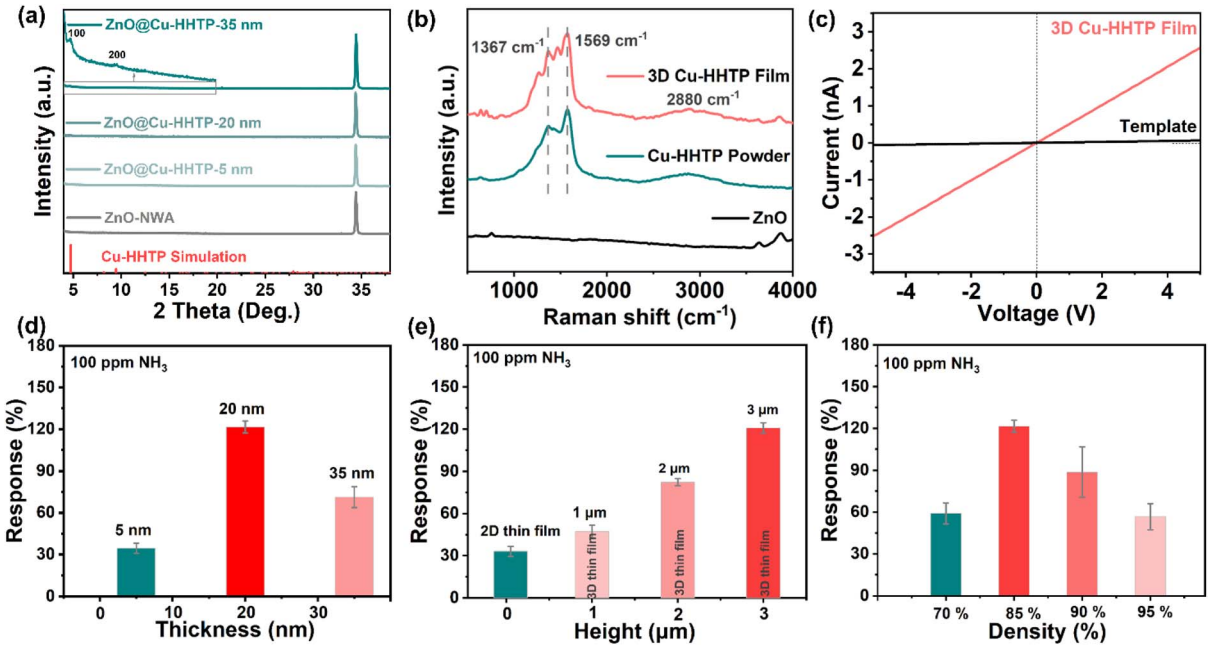

Fig. 3 (a) PXRD of 3D Cu-HHTP with different thicknesses grown on ZnO-NWA templates; (b) Raman spectra of the 3D Cu-HHTP thin film, Cu-HHTP powder, HHTP and ZnO-NWAs; (c) *I*–*V* of the 3D Cu-HHTP thin film and ZnO-NWA template. RT gas-sensing performances of 3D Cu-HHTP films: (d) responses to 100 ppm NH_3 with different thicknesses (the height is ~3 μm and the density is 85%); (e) responses to 100 ppm NH_3 with different heights (the thickness is 20 μm and the density is 85%); (f) responses to 100 ppm NH_3 with different densities (the height is ~3 μm and the thickness is 20 nm).

greater difficulty for gas diffusion, which decreases the sensitivity. These results were consistent with the prediction from our finite element method simulation model. It is important to note that there may be some differences between the experimental and theoretical results due to the inherent errors in both experiments and calculations. However, considering these factors, the observed trends are still understandable and provide valuable insights into the relationship between the microstructure of the Cu-HHTP 3D thin film and its gas sensing performance.

Based on the above results, a 20 nm thickness of the Cu-HHTP 3D thin film with the best gas sensing performance was selected to further study the influence of height and density on mass transport. It was found that the response to 100 ppm NH_3 increased with the increased height of the Cu-HHTP 3D thin film (Fig. 3e and S12†). The improved response was attributed to the increase in gas adsorption sites resulting from the increased height of the Cu-HHTP 3D thin film, which is consistent with the result of the calculation (Fig. 1a). The density of the Cu-HHTP 3D thin film is also a key factor affecting mass transport in gas sensing. To explore the effect of the density of the Cu-HHTP 3D thin film on gas sensing performance, ZnO-NWA templates with different densities ranging from 70%–90% were obtained to coat the Cu-HHTP thin film with a thickness of 20 nm (Fig. S4–S6†). The results of the gas sensing test showed that the response to 100 ppm NH_3 displays a Gaussian distribution with a maximum for the 85% density of the Cu-HHTP 3D thin film (Fig. 3f and S13†). Although the gas adsorption sites increased when the density of the Cu-HHTP 3D thin film changed from 85% to 90%, the difficulty of gas diffusion increased, leading to a decrease in gas sensing performance (Fig. 3f). The effect of the density of the Cu-HHTP 3D thin film on mass transport in gas sensing was also consistent with the calculation. Therefore, controlling mass transport through microstructure changes in terms of different thicknesses, heights and densities could effectively improve the gas sensing performance of the Cu-HHTP 3D thin film. Finally, Fig. 4a shows the typical concentration-dependent response–recovery curves of the 3D Cu-HHTP film with a thickness of ~20 nm, a height of ~3 μm and a density of ~85%, demonstrating its good response–recovery ability in a broad concentration range (1–100 ppm) of NH_3. The good linearity (R^2 = 0.99) is consistent with those of typical chemiresistive gas sensors (Fig. 4b). The theoretical limit of detection (LOD) of the Cu-HHTP 3D thin film is 0.78 ppm by setting the response to 10%. The response and recovery times of this device were estimated to be 1.85 min and 12.4 min (Fig. 4c). Besides, this device presented a better selectivity to NH_3 against 9 commonly existing interfering gases (Fig. 4d).

According to the results of the sensing test and reported literature,[37,38] the possible sensing mechanism of the Cu-HHTP 3D thin film is proposed (Fig. S14†): (1) upon exposure to NH_3, the porous structure of Cu-HHTP could effectively enrich the gas and the open metal sites serve as sensing functional motifs. (2) The metal sites function as Lewis acid sites to accept lone pair electrons from NH_3, reducing the number of holes and decreasing conductivity. (3) When exposed to bare air, NH_3 is removed to restore conductivity.

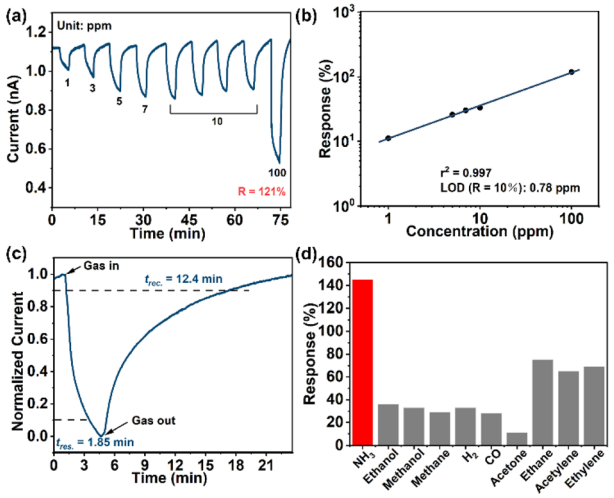

Fig. 4 Response–recovery curve (a), concentration–response log–log plots (b), response and recovery times (c), and selectivity (d) of the Cu-HHTP 3D thin film with a thickness of 20 nm, a height of ~3 μm and a density of 85%. The Cu-HHTP 3D thin film with a thickness of ~20 nm, a height of ~3 μm and a density of ~85% showed the best response to 100 ppm NH_3 (121%) in this work, which is considered to be at a moderate level for room temperature chemiresistive NH_3 sensors (Table S3†).

Conclusions

To reveal the relationship between the microstructure of 3D thin films and mass transport efficiency, a finite element method simulation model was developed to guide the preparation of Cu-HHTP 3D thin films with varying microstructures. These films were grown epitaxially on ZnO-NWAs, resulting in variations in thicknesses (0, ~5, ~20 and ~35 nm), heights (0.05, ~1, ~2 and ~3 μm) and densities (70%, 85%, 90% and 95%). The NH_3 sensing of these Cu-HHTP 3D thin films was tested to validate the predictions of the theoretical model. It is noteworthy that the Cu-HHTP 3D thin film with a thickness of ~20 nm, a height of ~3 μm, and a density of 85% exhibited the best performance, showing a response of ~120% towards 100 ppm NH_3, which is 4 times higher than those of Cu-HHTP 2D thin films prepared in this study. This work not only highlights the importance of the microstructure for gas sensing performance but also provides a feasible approach for designing MOF 3D thin films for other advanced applications involving heterogeneous reactions.

Data availability

The data that support the findings of this study are available from the corresponding author upon reasonable request.

Author contributions

Yu Pan: synthesis, characterization of Cu-HHTP 3D thin films, gas sensing, data curation, formal analysis, investigation, visualization, methodology and writing – original draft. Wei Sun: calculation, results analysis, visualization, and methodology. Jun-Xiang Chen: calculation and analysis of results. Yong-Jun Chen: conceptualization, data curation, formal analysis, investigation, writing – original draft, writing – review & editing, and funding acquisition. Zhen-Hai Wen: conceptualization, methodology, supervision, project administration and funding acquisition. Gang Xu: conceptualization, formal analysis, investigation, writing – review & editing, and funding acquisition.

Conflicts of interest

There are no conflicts to declare.

Acknowledgements

This work was financially supported by the Project Funded by the China Postdoctoral Science Foundation (2023M743496), the Postdoctoral Fellowship Program of CPSF under Grant Number GZC20241722, the National Natural Science Foundation of China (91961115, 22325109, 22171263, and 62227815), the Scientific Research and Equipment Development Project of CAS (YJKYQ20210024), the Fujian Science & Technology Innovation Laboratory for Optoelectronic Information of China (2021ZR101), the Natural Science Foundation of Fujian Province (2021J02017) and the Self-deployment Project Research Program of Haixi Institutes, Chinese Academy of Sciences (CXZX-2022-GH09).

Notes and references

1 S. Kitagawa, R. Kitaura and S. i. Noro, *Angew. Chem., Int. Ed.*, 2004, **43**, 2334.
2 H. C. Zhou, J. R. Long and O. M. Yaghi, *Chem. Rev.*, 2012, **112**, 673.
3 V. Stavila, A. A. Talin and M. D. Allendorf, *Chem. Soc. Rev.*, 2014, **43**, 5994.
4 P. Dong, X. Zhang, W. Hiscox, J. Liu, J. Zamora, X. Li, M. Su, Q. Zhang, X. Guo and J. McCloy, *Adv. Mater.*, 2023, 2211841.
5 H. Furukawa, K. E. Cordova, M. O'Keeffe and O. M. Yaghi, *Science*, 2013, **341**, 1230444.
6 I. Stassen, N. Burtch, A. Talin, P. Falcaro, M. Allendorf and R. Ameloot, *Chem. Soc. Rev.*, 2017, **46**, 3185.
7 N. Wang, Q. Sun and J. Yu, *Adv. Mater.*, 2019, **31**, 1803966.
8 X. Lin, D. Song, T. Shao, T. Xue, W. Hu, W. Jiang, X. Zou and N. Liu, *Adv. Funct. Mater.*, 2023, 2311637.
9 C. Lu, B. Clayville, J. Y. Choi and J. Park, *Chem*, 2023, **9**, 2757.
10 M. Wang, H. Shi, P. Zhang, Z. Liao, M. Wang, H. Zhong, F. Schwotzer, A. S. Nia, E. Zschech and S. Zhou, *Adv. Funct. Mater.*, 2020, **30**, 2002664.
11 Z. Chang, M. Zhu, Y. Sun, F. He, Y. Li, C. Ye, Y. Jin, Z. Li and W. Xu, *Adv. Funct. Mater.*, 2023, 2301513.
12 L. Zhao, J. Yan, H. Huang, X. Du, H. Chen, X. He, W. Li, W. Fang, D. Wang and X. Zeng, *Adv. Funct. Mater.*, 2023, 2310902.
13 X. C. Zhou, C. Liu, J. Su, Y. F. Liu, Z. Mu, Y. Sun, Z. M. Yang, S. Yuan, M. Ding and J. L. Zuo, *Angew. Chem., Int. Ed.*, 2023, **62**, e202211850.

14 Z. Li, J. Liu, X. Yi, W. Wu, F. Li, Z. Zhu, H. Li, J. Shi, Y. Xu and F. Zhou, *Adv. Funct. Mater.*, 2022, **32**, 2109541.
15 C. W. Kung, K. Otake, C. T. Buru, S. Goswami, Y. Cui, J. T. Hupp, A. M. Spokoyny and O. K. Farha, *J. Am. Chem. Soc.*, 2018, **140**, 3871.
16 R. Toyoda, N. Fukui, D. H. L. Tjhe, E. Selezneva, H. Maeda, C. Bourgès, C. Meng Tan, K. Takada, Y. Sun, I. Jacobs, K. Kamiya, H. Masunaga, T. Mori, S. Sasaki, H. Sirringhaus and H. Nishihara, *Adv. Mater.*, 2022, **34**, 2106204.
17 Y. Lu, Y. Zhang, C. Y. Yang, S. Revuelta, H. Qi, C. Huang, W. Jin, Z. Li, V. Vega-Mayoral and Y. Liu, *Nat. Commun.*, 2022, **13**, 7240.
18 T. Lee, J. O. Kim, C. Park, H. Kim, M. Kim, H. Park, I. Kim, J. Ko, K. Pak and S. Q. Choi, *Adv. Mater.*, 2022, **34**, 2107696.
19 J. Tang and Y. Yamauchi, *Nat. Chem.*, 2016, **8**, 638.
20 F. Cao, M. Zhao, Y. Yu, B. Chen, Y. Huang, J. Yang, X. Cao, Q. Lu, X. Zhang and Z. Zhang, *J. Am. Chem. Soc.*, 2016, **138**, 6924.
21 P. Pachfule, D. Shinde, M. Majumder and Q. Xu, *Nat. Chem.*, 2016, **8**, 718.
22 W. H. Li, K. Ding, H. R. Tian, M. S. Yao, B. Nath, W. H. Deng, Y. Wang and G. Xu, *Adv. Funct. Mater.*, 2017, **27**, 1702067.
23 Z. Zhou, S. Mukherjee, S. Hou, W. Li, M. Elsner and R. A. Fischer, *Angew. Chem., Int. Ed.*, 2021, **60**, 20551.
24 W. T. Koo, J. S. Jang and I. D. Kim, *Chem*, 2019, **5**, 1938.
25 M. S. Yao, X. J. Lv, Z. H. Fu, W. H. Li, W. H. Deng, G. D. Wu and G. Xu, *Angew. Chem., Int. Ed.*, 2017, **56**, 16510.
26 R. Dong, T. Zhang and X. Feng, *Chem. Rev.*, 2018, **118**, 6189.
27 E. Virmani, J. M. Rotter, A. Mähringer, T. Von Zons, A. Godt, T. Bein, S. Wuttke and D. D. Medina, *J. Am. Chem. Soc.*, 2018, **140**, 4812.
28 Y. Liu, Y. Wei, M. Liu, Y. Bai, X. Wang, S. Shang, J. Chen and Y. Liu, *Angew. Chem., Int. Ed.*, 2021, **60**, 2887.
29 A. Schneemann, V. Bon, I. Schwedler, I. Senkovska, S. Kaskel and R. A. Fischer, *Chem. Soc. Rev.*, 2014, **43**, 6062.
30 X. Ma, Y. Chai, P. Li and B. Wang, *Acc. Chem. Res.*, 2019, **52**, 1461.
31 M. E. DMello, N. G. Sundaram, A. Singh, A. K. Singh and S. B. Kalidindi, *Chem. Commun.*, 2019, **55**, 349.
32 M. G. Campbell, S. F. Liu, T. M. Swager and M. Dinca, *J. Am. Chem. Soc.*, 2015, **137**, 13780.
33 Y. Lin, W. H. Li, Y. Wen, G. E. Wang, X. L. Ye and G. Xu, *Angew. Chem., Int. Ed.*, 2021, **60**, 25758.
34 R. Zheng, Z. H. Fu, W. H. Deng, Y. Wen, A. Q. Wu, X. L. Ye and G. Xu, *Angew. Chem., Int. Ed.*, 2022, **61**, e202212797.
35 W. Zhan, Q. Kuang, J. Zhou, X. Kong, Z. Xie and L. Zheng, *J. Am. Chem. Soc.*, 2013, **135**, 1926.
36 M. S. Yao, W. X. Tang, G. E. Wang, B. Nath and G. Xu, *Adv. Mater.*, 2016, **28**, 5229.
37 V. Rubio-Giménez, N. Almora-Barrios, G. Escorcia-Ariza, M. Galbiati, M. Sessolo, S. Tatay and C. Martí-Gastaldo, *Angew. Chem.*, 2018, **130**, 15306.
38 R. M. Stolz, A. Mahdavi-Shakib, B. G. Frederick and K. A. Mirica, *Chem. Mater.*, 2020, **32**, 7639.